A&A 670, A11 (2023)
https://doi.org/10.1051/0004-6361/202244288

Astronomy & Astrophysics

Dynamical state of the globular clusters Rup 106 and IC 4499

G. Beccari[1], M. Cadelano[2,3], and E. Dalessandro[3]

[1] European Southern Observatory, Karl-Schwarzschild-Strasse 2, 85748 Garching bei München, Germany
e-mail: gbeccari@eso.org
[2] Dipartimento di Fisica e Astronomia "Augusto Righi", Universitá degli Studi di Bologna, Via Gobetti 93/2, 40129 Bologna, Italy
[3] INAF-Astrophysics and Space Science Observatory Bologna, Via Gobetti 93/3, 40129 Bologna, Italy

Received 16 June 2022 / Accepted 12 November 2022

ABSTRACT

The dynamical evolution of globular clusters is theoretically described by a series of well-known events typical of N-body systems. Still, the identification of observational signatures able to empirically describe the stage of dynamical evolution of a stellar system with a density typical of a globular cluster represents a challenge. In this paper, we study the dynamical age of the globular clusters Rup 106 and IC 4499. To this aim, we study the radial distribution of the blue straggler stars (BSSs) via the A^+ parameter and of the slope of the main sequence mass function. Both tracers show that Rup 106 and IC 4499 are dynamically young clusters where dynamical friction has just started to segregate massive stars towards their respective centres. Furthermore, we observe that the BSSs are more centrally concentrated in both clusters than the reference population. Similarly, we find that in both cases the slope of the mass function significantly decreases as a function of the cluster-centric distance. This result provides additional support for the use of the radial distribution of the BSSs as a powerful and observationally convenient indicator of the cluster dynamical age.

Key words. blue stragglers – globular clusters: individual: Rup 106 – globular clusters: individual: IC 4499 – stars: kinematics and dynamics

1. Introduction

Globular clusters (GCs) are the oldest (∼12 Gyr), most massive (10^4–10^6 $M_\odot$), and densest stellar aggregates in the Galaxy. They are populated by millions of stars, whose age, distance, and chemical composition can be determined with high accuracy. For this reason, GCs play a crucial role in our current understanding of stellar and dynamical evolution. During their long life, GCs experience all the most relevant dynamical events foreseen in an N-body system, such as gravothermal instability, violent relaxation, energy equipartition, two-body and higher order collisions, binary formation and heating, and 'erosion' via tidal interaction with external fields (Meylan & Heggie 1997). The internal dynamics of such massive stellar aggregates affect objects of all masses and can be efficiently probed by means of massive test particles, such as binaries, millisecond pulsars, and blue straggler stars (BSSs; e.g., Bailyn 1995; Beccari et al. 2006; Prager et al. 2017; Mapelli 2018; Singh & Yadav 2019). These latter are perhaps most often used for this purpose because they are numerous and relatively easy to detect (e.g., Ferraro et al. 2012, 2018).

Blue straggler stars are the by-product of the complex interplay between cluster dynamics and stellar evolution. They are defined as stars hotter (and therefore bluer) and brighter than main sequence turnoff (MSTO) stars within a cluster. BSSs form either through mass transfer (Leonard 1996) or collision events (Lombardi et al. 1995). Both formation channels are expected to work simultaneously within a given cluster (Knigge et al. 2009; Ferraro et al. 2009; Dalessandro et al. 2013). However, the relative importance of each process likely depends on the physical properties of the parent cluster (e.g., Sollima et al. 2008; Leigh et al. 2013; Sills et al. 2013). Independently of their formation mechanism, BSSs are a population of heavy objects (∼1–1.6 $M_\odot$) orbiting in a sea of stars that are three to four times less massive. For this reason, BSSs can be used as powerful gravitational probe particles to investigate key dynamical processes (such as mass segregation) characterising the dynamical evolution of star clusters. In a series of papers (Ferraro et al. 2012, 2018; Lanzoni et al. 2016), our group showed that the morphology of the BSS radial distribution is shaped by the action of dynamical friction (DF), which drives the objects that are more massive than the average towards the cluster centre, with an efficiency that decreases with increasing radial distance.

Driven by the same physical processes, the radial variation of the luminosity function (LF) and mass function (MF) of MS stars can provide information about the effect of cluster internal dynamics on stars in a wide range of masses, including the faint end of the MS, where most of the cluster mass lies. In relaxed stellar systems, the slope of the MF is expected to vary as a function of the distance from the cluster centre, with indexes decreasing as the distance increases, because of the differential effect of mass segregation (Webb et al. 2017; Cadelano et al. 2020).

Here we present an analysis of the dynamical state of the GCs IC 4499 and Ruprecht 106 (hereafter Rup 106). We used photometric catalogues obtained by combining *Hubble* Space Telescope (HST) and ground-based wide field data. The vast data set allows us to resolve the stellar population of the clusters from the very centre to the their outer regions.

IC 4499 is a low-density (c = 1.21) cluster in the southern hemisphere at RA = 15h00m18.45s, Dec = −82h12m49.3s, lying in the intermediate to outer Galactic halo at a distance of 15.7 kpc from the Galactic centre (Harris 1996, 2010 edition). This cluster aroused attention in the past due to its high frequency of variable stars (Walker & Nemec 1996), large number of BSSs (Dotter et al. 2011), and for having been suggested as one of the very few GCs not showing evidence

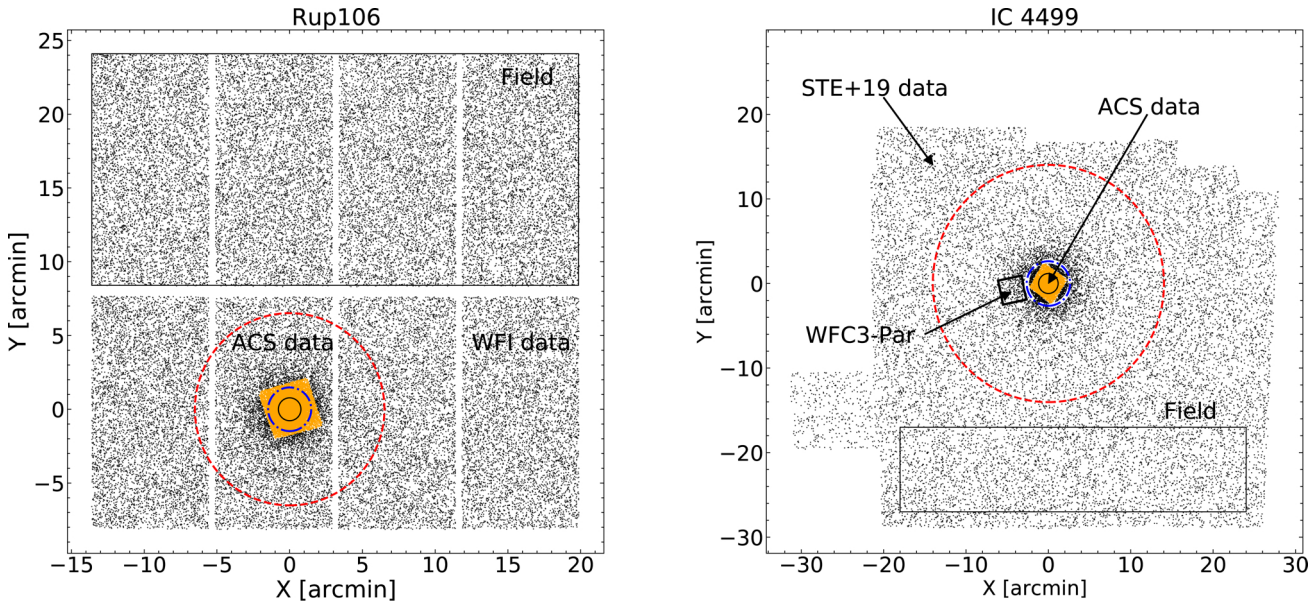

Fig. 1. Data FoV. Composite FOVs showing the stars sampled in Rup 106 (*left panel*) and IC 4499 (*right panel*). The central field identifies the stars sampled with the ACS catalogues (orange points). The solid (black), dot-dashed (blue), and dashed (red) circles mark the core, half-mass, and tidal radii of the clusters, respectively. The area used to estimate the field contamination and the area covered by the WFC3 parallel observations are also labelled.

of multiple populations with light-element abundance variations (but see Dalessandro et al. 2018). Ferraro et al. (1995) suggested an unusual, 3–4 Gyr younger age for this cluster compared to clusters with similar metallicity, but this result was contradicted by Dotter et al. (2011) who suggested an age of 12.0 ± 0.75 Gyr and [Fe/H] ~ -1.6.

Rup 106 is a low-mass ($3.4 \times 10^4\ M_\odot$ Baumgardt et al. 2019), metal-poor GC lying about 25 kpc from the Galactic centre and was first examined by Buonanno et al. (1990, 1993). Similarly to IC 4499, Rup 106 was suggested (Buonanno et al. 1993) to be 4–5 Gyr younger than GCs with similar metallicity. More recently, Dotter et al. (2011) suggested an age of 11.5 Gyr with [Fe/H] ~ -1.5 while Villanova et al. (2013) demonstrated that Rup 106 is one of the few GCs that convincingly does not show evidence of the presence of multiple stellar populations (see also Frelijj et al. 2021).

Moreover, Fusi Pecci et al. (1995) suggest that both IC 4499 and Rup 106 are possibly members of a tidal stream around the Milky Way. Recently, Massari et al. (2019), using *Gaia* DR2 data, found that IC 4499 is likely associated with the Sequoia galaxy merging event, while similarly, Rup 106 is associated with the progenitor of the Helmi stream.

In Sect. 2, we present the observations and the data reduction process we used. We derive the structural parameters of the clusters in Sect. 3, and in Sect. 4 we use the radial distribution of the BSSs of the clusters to investigate their dynamical state. Finally, we investigate the degree of mass segregation in the two clusters imprinted in the radial distribution of the slope of the MF (Sect. 5).

2. Observations and data reduction

The main scope of this paper is to empirically investigate the dynamical state of the GCs Rup 106 and IC 4499 using the radial distribution of BSSs and any radial change of the slope of the MF (α). Both approaches require a data set able to sample the stellar population in both clusters over a comparable physical area.

To this aim, we used a combination of ground-based wide-field images to sample the brightest populations of the clusters from their central regions to their tidal radii (r_t) and deep high-resolution images acquired with the Advanced Camera for Survey (ACS) on board the HST to sample the MS stars in the very low-mass regime out to the half-mass radius (r_h) of each cluster.

Rup 106 and IC 4499 were both observed with the ACS under the HST Proposal 11586 (PI Dotter). The clusters were imaged with their cluster core positioned at the centre of the ACS field of view (FoV) in the F606W (V band) and F814W (I band) filters for total exposure times of 2250 s and 2340 s (Rup 106), and 2412 s and 2544 s (IC 4499), respectively. A dithering pattern was adopted in both cases to fill the gaps in the ACS CCD mosaic. The ACS data alone allow us to sample the MS stars of Rup 106 out to $r_h = 88\farcs83$ (dash-dotted circle in Fig. 1; see also Sect. 3).

IC 4499 has $r_h = 158\farcs15$, which falls out of the ACS FoV (see Fig. 1). In this case, we also retrieved a set of images from the HST archive taken with the Wide Field Camera 3 (WFC3) as part of HST parallel observations. In particular, 2×600 s and 2×800 s parallel observations with the $F606W$ and $F814W$ filters were obtained with the WFC3 via the HST Proposal 14235 (PI Sohn) to observe the external region of IC 4499. These parallel observations allow us to sample the MS stars in IC 4499 outside of the core region and beyond the r_h, as in the case of Rup 106.

In order to sample the brightest stars in Rup 106, we complemented the ACS sample with a catalogue obtained using a number of wide-field images acquired under the program 71.D-0220(A), (PI: Ortolani) with the Wide Field Imager (WFI) at the MPE2.2m telescope (La Silla) using the V89_ESO843 and IcIwp_ESO845 filters (hereafter V and I, respectively). Thanks to its wide FoV ($34' \times 34'$) and resolution ($0\farcs234$), the WFI camera allowed us to sample the brightest stellar population of Rup 106 in a region well beyond its r_t. Finally, we used the wide-field catalogue of IC 4499 published by (Stetson et al. 2019), which offers a complete star sample out to a radius of $842''$ or $14'$. The catalogue combines a sample of images from various telescopes and was previously used by Walker et al. (2011) to

Table 1. Log of the observations.

Data-set	Number of exposures	Filter	Exposure time (s)
	Rup 106		
WFI	2	V	200
	2	I	180
ACS	4	V_{606}	550
	4	I_{814}	585
	IC 4499		
ACS	4	V_{606}	603
	4	I_{814}	636
WFC3	2	V_{606}	600
	2	I_{814}	800

study the formation history of IC 4499. A detailed description of the images adopted to create the photometric catalogue is available in Table 1 of Stetson et al. (2019, hereafter STE19).

Table 1 provides a summary of the observations adopted in this work. Figure 1 shows the maps of the surveyed areas around Rup 106 (left panel) and IC 4499 (right panel). The locations of the different data sets in the FoV are labelled in the figures. We use the ground-based catalogues alone to calculate the radial density profiles of the clusters and estimate their structural parameters. The ACS catalogues combined with the ground-based catalogues are used to study the radial distribution of the BSSs in the two clusters (Sect. 3). To this purpose, the we use the ground-based catalogues to sample the stellar population outside the FoV of the ACS data (see Fig. 1). Finally, the ACS catalogues and the WFC3 parallel observations in the case of IC 4499 are used to measure how the slope of the MFs changes as a function of the distance from the cluster centres (Sect. 5).

2.1. Data reduction

We retrieved the ACS and WFC3 `flc` images from the Mikulski Archive for Space Telescopes (MAST)[1]. The images are calibrated and corrected for loss of charge transfer efficiency (CTE). We also downloaded the raw WFI images together with the BIAS and FLAT-FIELD images from the ESO archive[2]. Flat-field and bias correction were performed with the data-reduction software Theli (Erben et al. 2005; Schirmer 2013).

We performed the data reduction of the HST (both ACS and WFC3) and WFI data sets through an accurate modelling of the point spread function (PSF) followed by a standard PSF-fitting procedure using `DAOPHOTII` (Stetson 1987, 1994). Briefly, we first used from 30 to 50 well-sampled and non-saturated stars in each image to model the PSF. We then used `DAOPHOTII/ALLFRAME` to perform the PSF fitting on the HST and WFI data sets, separately. The magnitude of each star included in the final photometric catalogues is the average of at least three measurements in each band, while we adopted the standard deviation as the associated photometric error.

The instrumental V, I magnitudes of the ACS sample were calibrated into the Johnson standard system using the recipe in Sirianni et al. (2005). Briefly, a sample of bright isolated stars was used to transform the instrumental magnitudes to a fixed aperture of 0.″5. An extrapolation to infinity was then performed using the values listed in Table 5 of Sirianni et al. (2005). The magnitudes were finally transformed into the Johnson system using Eq. (12) from Sirianni et al. (2005).

For a sanity check, Fig. 2 shows the difference between the calibrated magnitudes of the stars in IC 4499 in common between the ACS and the STE19 catalogues. The plots demonstrate that, using the calibration recipe described in Sirianni et al. (2005), we achieve an excellent photometric homogeneity. Still, the best-fit lines (dashed lines) indicate that there is a residual difference of 0.037 and 0.021 mag in V and I respectively, between the ACS and the STE19 photometry. Such a small residual offset is due to the difference between the zero-points from Sirianni et al. (2005) and the latest implemented by the ACS Team[3]. We therefore decided to apply such offsets to the ACS catalogue in order to obtain homogeneous V and I magnitudes between the ACS and the STE19 data sets. Similarly, adopting the zero-point available on the HST web pages[4] we calibrated the instrumental magnitudes of the stars detected in the WFC3 data into VEGAMAG. We then used more than 100 stars in common with the STE19 catalogue to calibrate the WFC3 catalogue against the STE19 photometry.

The calibration of the WFI catalogue of Rup 106 was done in two steps. First, we calibrated the V and I magnitudes of the WFI catalogue using 1174 stars in common with the UCAC4 catalogue (Zacharias et al. 2012). This first step allowed us to obtain a homogeneous calibration over the entire WFI FoV. We then transformed the magnitude of the stars of the WFI photometric catalogue into the ACS-Johnson system using more than 200 stars in common between the ACS and WFI catalogues.

We obtained an absolute astrometric solution for the stars in both the ACS and the WFI catalogue using several hundred stars in common with the *Gaia*-DR2 catalogue (Gaia Collaboration 2016, 2018). The final rms global accuracy is of 0.″3, in both right ascension (α) and declination (δ).

Figure 3 shows the colour–magnitude diagrams (CMDs) of the cluster Rup 106 (two plots on the left-hand side) and IC 4499 (two plots on the right-hand side). We report at the top of each panel the name of the cluster and the adopted data set while the MS mean-ridge calculated on the HST data is shown as a red solid vertical line for both clusters. Clearly, the ACS catalogue allows us to sample the stars of the two clusters from the population of BSSs sampled in a region almost 2 mag brighter with respect to the clusters' MSTO ($V_{\rm TO} \sim 21$), down to the very low-mass end of the MS at $V \sim 29$. On the other hand, the ground-based catalogue samples the stars of the clusters below the MSTO and well beyond the clusters' $r_{\rm t}$.

2.2. Artificial stars experiment

In this work, we use detailed star counts to calculate the radial density profiles of the clusters and derive their physical parameters (Sect. 3). Also, we observationally investigate the dynamical status of Rup 106 and IC 4499 using the radial distribution of the BSSs (Sect. 4) and that of the slope of the clusters' MF (Sect. 5). It is therefore important to quantitatively assess the quality of the data in terms of completeness of the sample. The latter is defined as the number of stars of each cluster that we lost during the reduction analysis described in Sect. 2.1 as a function of the stellar magnitudes and radial position in the cluster.

[1] https://archive.stsci.edu/
[2] http://archive.eso.org
[3] https://www.stsci.edu/hst/instrumentation/acs/data-analysis/zeropoints
[4] https://www.stsci.edu/hst/instrumentation/wfc3/data-analysis/photometric-calibration

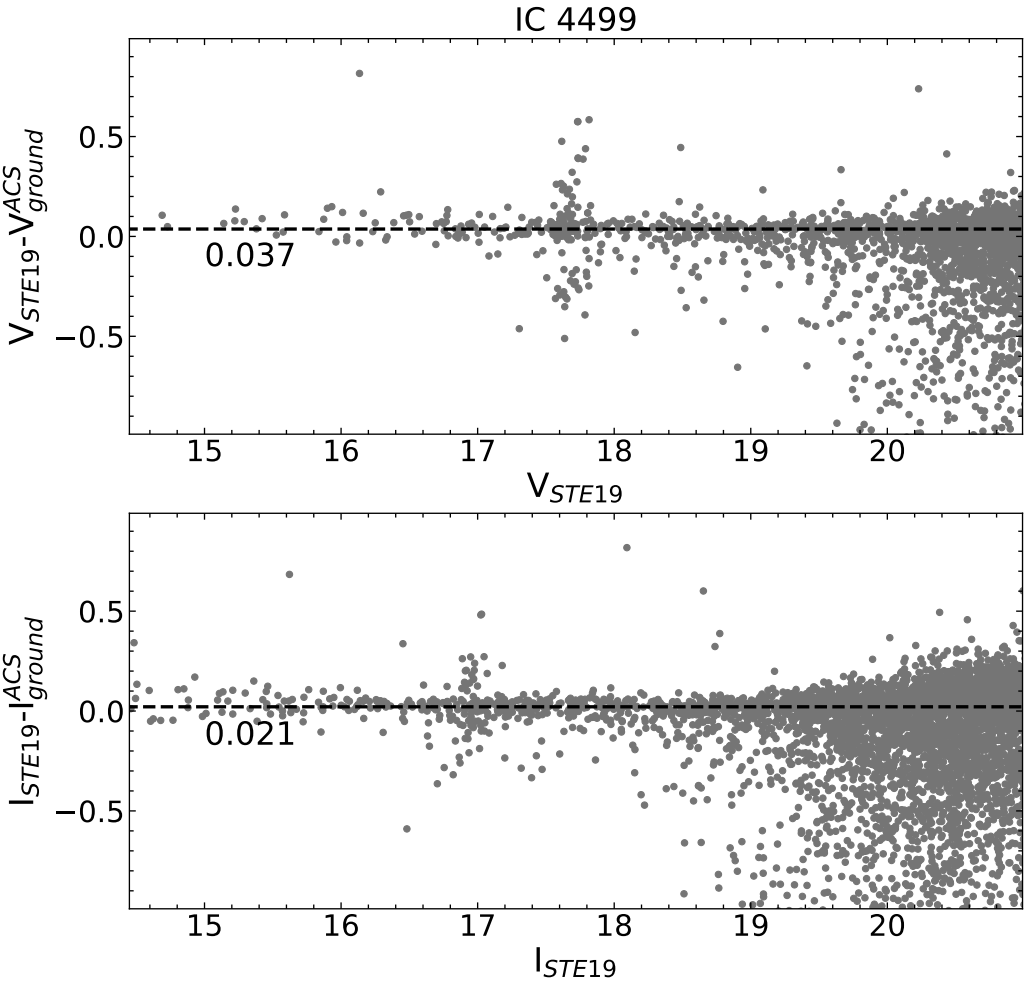

Fig. 2. Photometric calibration. Comparison between the *V* and *I* (upper and lower panels, respectively) photometry of IC 4499 calibrated into the Johnson photometric system for the stars in common between the ACS and the photometric catalogue of Stetson et al. (2019). The horizontal line shows the best linear fit to the observed distribution.

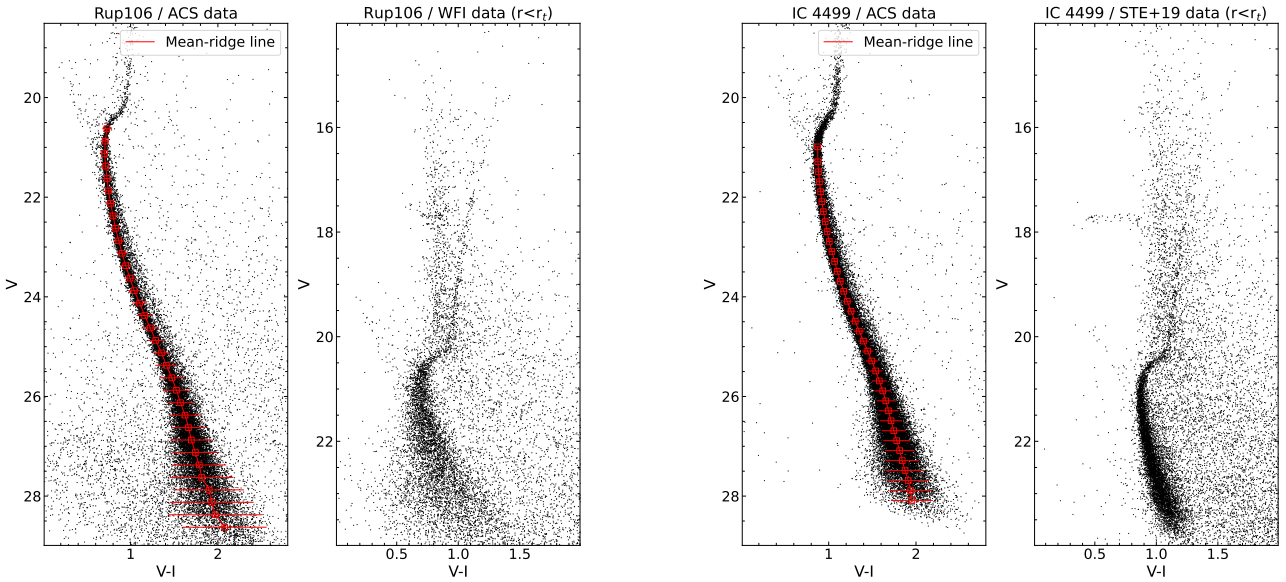

Fig. 3. Colour–magnitude diagrams for Rup 106 (two plots on the left-hand side) and IC 4499 (two plots on the right-hand side). The MS mean-ridge calculated on the HST data is shown as a red solid vertical line for both clusters.

We study the photometric completeness of the HST data set following the recipe described in Bellazzini et al. (2002); we use this data set to study the MF of the clusters. As we explain below, we assess the completeness of the ground-based photometry from the HST catalogues.

First, we created a catalogue of artificial stars. The V magnitudes of these stars were extracted from the observed LFs of the clusters, which themselves were derived using the HST data. We artificially increase the number of stars towards the low-luminosity, low-magnitude regimes. This is done in order to not overpopulate the images with bright stars while at the same time well-sampling the low-magnitude regimes, where a solid statistical sample of simulated stars is crucial to assess the fraction of stars lost during the data-reduction process. The I magnitude is assigned via the $V - I$ colour obtained by interpolating each V magnitude using the clusters MS mean-ridge line (see red solid lines in Fig. 3). Then, we add the stars on each V and I HST image, adopting their specific PSF models using the routine `DAOPHOTII/ADD`. Once the images with the artificial stars are created, we follow the same data-reduction strategy described in Sect. 2.1. At the end of the data-reduction process, a star is only considered recovered if it was successfully measured in both magnitudes as for the real stars and if the difference between the assigned magnitude (input) and the one measured after the PSF fitting process (output) is <0.75 (both in V and I, independently). A star showing a larger difference in one of the magnitudes is considered to be an unresolved blended source and hence undetected (Bellazzini et al. 2002). We stress here that stars are randomly placed on the FoV covered by the HST images following a regular grid such that a minimum distance equal to three times the full width at half maximum (FWHM) is guaranteed between two simulated stars. This is critical in order to avoid introducing artificial stellar crowding to the images. The experiments are repeated until a total of 100 000 stars is simulated in each ACS pointing and about 60 000 in the WFC3 parallel ones.

Figure 4 shows the photometric completeness of the data (ϕ) calculated as the ratio between the number of artificial stars injected into the images and the ones recovered as a function of the V magnitude and at different radial annuli from the cluster centres. The radial ranges covered by the annuli are reported in arcseconds in the figure. The errors of the completeness value of each star (σ_ϕ) were computed by propagation of the Poissonian errors. A value of $\phi = 1$ indicates 100% recovery rate. We indicate with a horizontal dashed line the lower limit of 50% (i.e., $\phi = 0.5$) recovery rate, below which the number of lost stars is too large to safely correct the observed star counts (and derive the MF). The quality of the HST data used in this work is such that we detect in both clusters the MS stars in a range of magnitude $24 \lesssim V \lesssim 21$ with a 100% level of completeness, while the completeness is always >80% in the range $27 \lesssim V \lesssim 24$.

We use the accurate study of photometric completeness done for the HST data to assess the quality of the catalogues obtained from ground-based photometry. As shown in Fig. 4, the HST data are 100% complete at magnitudes $V \lesssim 21$. We can therefore use all the stars sampled by the HST data in this regime of magnitudes as a reference catalogue and estimate how many stars with magnitude $V \lesssim 21$ we recover with the ground-based photometry. In particular, we find that in the magnitude regimes $21 \lesssim V \lesssim 20$ and $20 \lesssim V \lesssim 19$, with the ground-based catalogues we respectively recover 80% and 95% of the stars sampled with the HST data with no significant difference with respect to the radial position. This is due to the fact that the completeness of the data is driven by the sensitivity towards faint magnitudes rather that severe stellar crowding, which is very low. This demonstrates that we can safely perform statistical studies based on star counts using both the HST and ground-based catalogues.

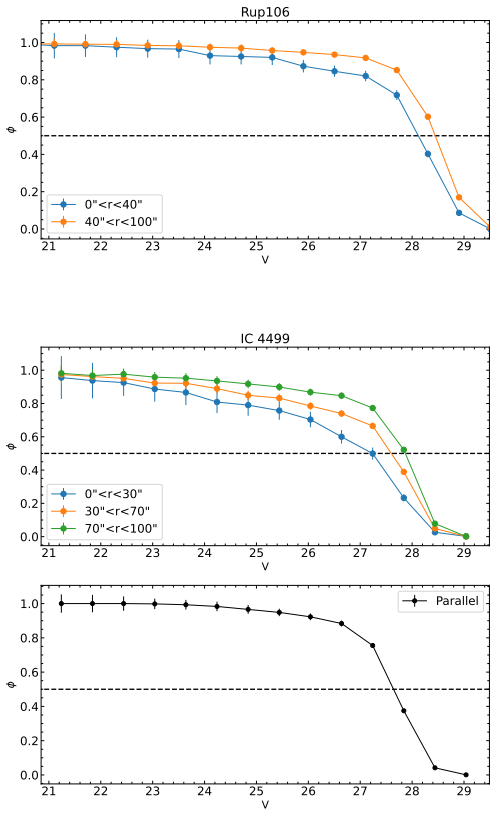

Fig. 4. Photometric completeness (ϕ) as a function of V for the ACS data of Rup 106 (*upper panel*) and for the ACS and WFC3 parallel observations of IC 4499 (*central* and *lower panels*).

3. Ground-based data set: the cluster's structural parameters

We can take advantage of the accurate sampling of the stellar populations in the clusters to determine the radial density profiles from the star counts. This can be done by following a standard procedure already adopted by Lanzoni & Ferraro (2019, and reference therein). Briefly, we first used the ground-based catalogues to estimate the cluster centres, calculated as the average position projected on the sky of the sampled stars from $V = 15$ down to $V = 20{,}20.5{,}21{,}21.5{,}22{,}22.5{,}23$. Moreover, we only use those stars within a half-mass radius from the cluster centre. At this stage, we adopted the values of the half-mass radius reported by Harris (1996, 2010 edition). The use of progressively fainter limiting magnitudes allows us to increase the number of sampled stars while mitigating possible effects related to the decreasing photometric completeness. The adopted centres are the average of the values obtained in the different magnitude bins and the dispersion represents the corresponding uncertainty. The coordinates of the centres are $\alpha_{J2000} = 12^{\rm h}38^{\rm m}40\overset{\rm s}{.}56, \delta_{J2000} = -51°09'01''58$ for Rup 106 and $\alpha_{J2000} = 15^{\rm h}00^{\rm m}16\overset{\rm s}{.}67, \delta_{J2000} = -82°12'49''47$ for IC 4499. The overall uncertainties are $\sim 2''$ and $\sim 1''$ in α and δ, respectively.

As a second step, we used the ground-based catalogues to derive the radial density profiles of the two clusters from the star counts. For each cluster, we build the profile by calculating the density of the stars in several annuli, all centred on the cluster

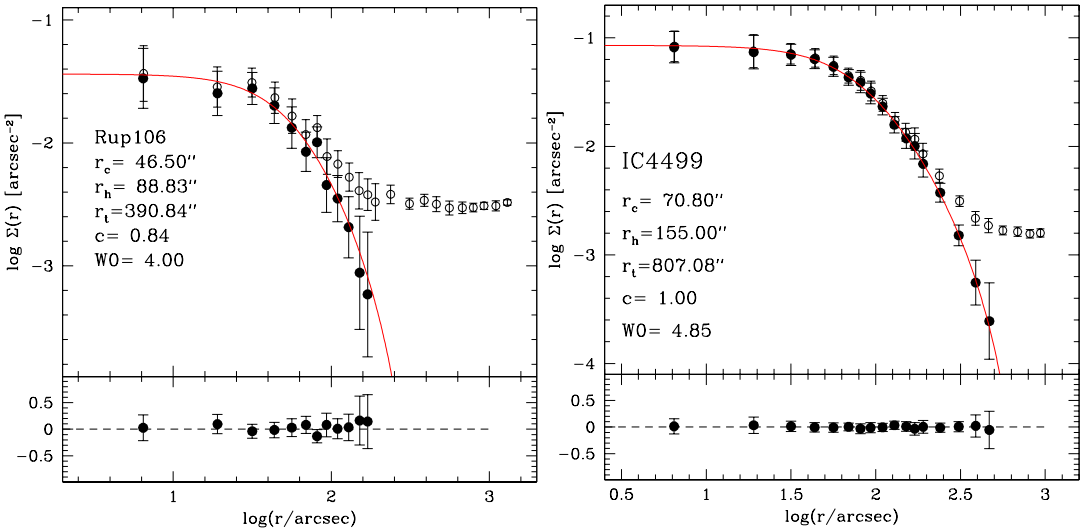

Fig. 5. Density profiles. The solid circles show the radial density profile of Rup 106 (*left panel*) and IC 4499 (*right panel*) corrected for the contamination from the background and foreground stars. The open circles indicate the background and foreground uncorrected counts. The density of field stars was estimated using the most external bins. The best-fit King model is shown as a solid line on the figures while the small panel at the bottom of the figures shows the residual of the fit at each radial bin. The parameters of the best-fit King model are also indicated in the figure.

centre. Specifically, we divide each annulus into four quadrants of identical size. The stellar density of the annulus is then the mean of the stellar density in the four individual quadrants, while the standard deviation is taken as the associated error. We used all the stars with magnitude $V < 21$. We show the observed density profiles of the clusters as open circles in Fig. 5.

The background-corrected profiles (solid circles in the figure) were fit with single-mass, spherical, and isotropic King models (King 1966), which constitute a single-parameter family, where the shape of the density distribution is uniquely determined by the value of the concentration parameter (c) or, equivalently, the value of W_0 that is linked with the dimensionless central potential. For each cluster, we compared the observed profile with a grid of King models with c varying between 0.8 and 2.5 in steps of 0.05 (Miocchi 2006). From the analysis of the residuals between the observed and the theoretical profiles, we then determined the best-fit solution as the model providing the minimum χ^2 value (see Lanzoni & Ferraro 2019 for more details). The best-fit models are shown as solid red lines in Fig. 5, where we also label the value of the main structural parameters. In both cases, we find very small values for the concentration parameter ($c = 0.84$ and 1.02 for Rup 106 and IC 4499, respectively) and large core radii ($r_c = 46.5''$ or 4.10 pc and 70.9″ or 6.46 pc, respectively), in agreement with the expectations for such low-density systems. Moreover, Rup 106 has a tidal radius $r_t = 390.''84$ (34.48 pc) and for IC 4499 we find that $r_t = 807.''08$ (73.56 pc). We estimate the size of the radii in parsecs by assuming distances of 21.20 Kpc and 18.8 Kpc for Rup 106 and IC 4499, respectively (Harris 1996, 2010 edition).

We note that the structural parameters that we derive in this work for the two clusters slightly differ from the ones reported by Harris (1996, 2010 edition) and the recent study done by Baumgardt & Hilker (2018). Arguably, the difference is due to the different data sets used in our work and by Baumgardt & Hilker (2018) to estimate the parameters. While our data allow us to sample the stellar population of the clusters well beyond r_t, Baumgardt & Hilker (2018) used HST archive data to sample mostly the central regions complemented with surface-brightness profiles to sample the external areas. We stress here that determining the radial density profiles from the star counts using properly resolved stars allows us to exclude any possible bias introduced by the presence of a few bright stars, which would significantly alter the location of the surface brightness maximum and possibly the precise shape of the profile itself (see also Lanzoni & Ferraro 2019). Moreover, as proven by Miocchi et al. (2013), the availability of wide-field catalogues that make it possible to sample the cluster stellar population for its total extension is essential in order to gain sufficient control of the level of background contamination.

4. Combined data set: radial distribution of the blue straggler population

As extensively shown in the literature, the population of BSSs and their radial distribution can be successfully used to investigate the dynamical age of a GGC. In GCs, BSSs are on average more massive (∼1.2 $M_\odot$; see e.g., Fiorentino et al. 2014; Raso et al. 2020) than the stars of the cluster, whose average mass is of the order of 0.3−0.4 $M_\odot$. As a consequence, BSSs sink to the centre because of dynamical friction. Indeed, when compared to the radial distribution of standard stellar populations in a GC (e.g., RGB), the BSSs are typically more centrally concentrated, suggesting that dynamical friction efficiently segregates BSSs towards the central potential well of the cluster (see e.g., Ferraro et al. 2012).

Ferraro et al. (2018) published a comparative study of the radial behaviour of the BSS population in 48 GCs, adopting the parameter A^+. Initially introduced by Alessandrini et al. (2016), the A^+ of a GC is defined as the area enclosed between the cumulative radial distribution of the population of BSSs of a given GC and that of a reference population (e.g., RGB or MSTO stars). This dimensionless parameter turns out to be a solid empirical indicator of the degree of segregation of the population of BSSs, with A^+ increasing as a function of the degree of sedimentation of the BSSs into the cluster centre. The parameter A^+ tightly correlates with the ratio of cluster age to the current central relaxation time,

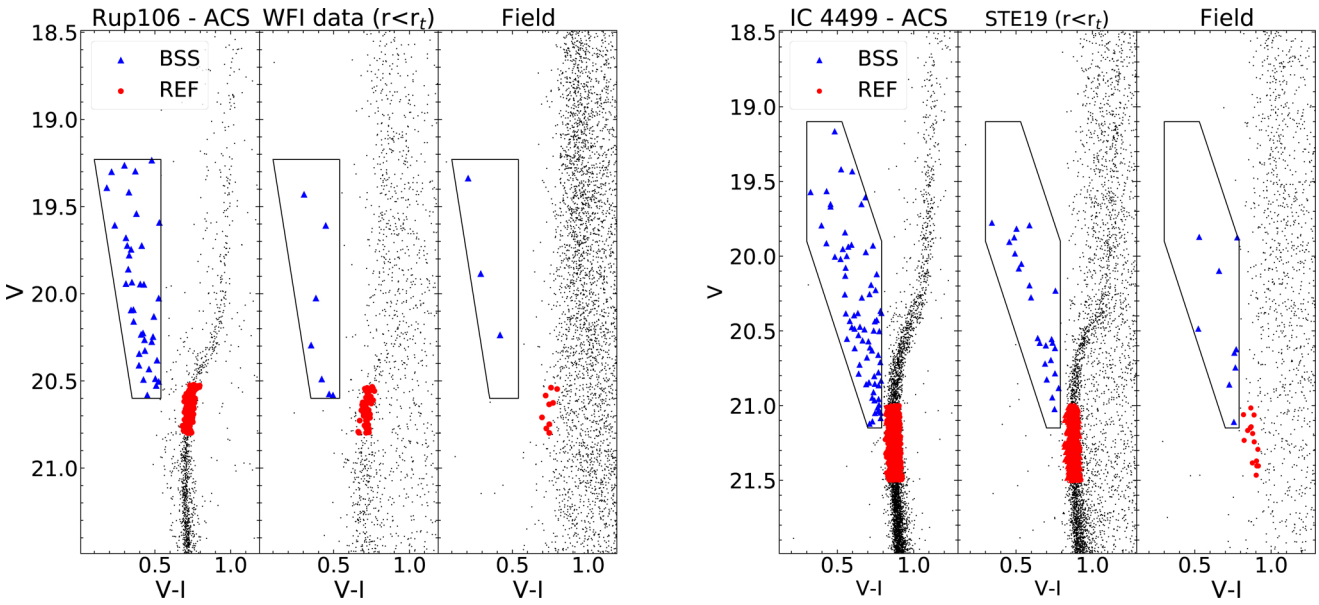

Fig. 6. Selection of the population of BSSs on the ACS and ground-based data sets of Rup 106 and IC 4499. The solid box empirically defines the BSS area. The selection boxes are homogeneously used to select BSSs (blue solid triangles) on all the catalogues. The stars along the MS turn-off (red solid circle) are used as a reference population.

making A^+ an efficient clock to empirically measure the dynamical age of GCs (see also Lanzoni et al. 2016).

Here, we aim to use the BSSs and the A^+ as an empirical clock to assess the dynamical ages of Rup 106 and IC 4499. As a first step, we select the population of bona fide BSSs in the CMDs of the clusters. The BSSs live along the MS in a position brighter and bluer with respect to the MSTO. Indeed, the BSS sequences of the two clusters are clearly visible in the CMDs shown in Fig. 3.

Following the definition of the population of BSSs given above, we empirically define a BSS selection box for Rup 106 and IC 4499 as shown in Fig. 6. The populations of BSSs in the two clusters are shown as blue solid triangles in the figures, while we adopt the stars at the MSTO (REF; red solid circles in the figure) as a reference population, sampling the distribution of the light in the clusters. The selection is homogeneously applied across both available data sets thanks to the fact that, as described in Sect. 2.1, for both GCs studied in this paper, the V and I magnitudes of all catalogues have been reported in the same photometric system. We selected a total of 56 BSS and 745 REF stars inside the r_t of Rup 106, while 98 and 1896 are found in IC 4499. In addition, given the radial extent of the ground-based data sets, we are able to provide a solid estimate of the contamination of BSS and REF stars by foreground and background stars, which turn out to be negligible for both clusters: less than one field star inside the r_h is expected among the population of BSS and REF stars for both clusters. We also note that, here, the MSTO of the clusters are located at $V \sim 21$ mag, which means they are too faint to allow us to use the *Gaia* early Data Release 3 catalogue to asses individual cluster membership based on robust astrometric information for the stars populating the BSS sequence.

Figure 7 shows the cumulative radial distribution of the population of BSS and REF stars in the clusters Rup 106 and IC 4499 (left and right hand panels, respectively). The cumulative distributions are derived with respect to the centre of each cluster obtained in Sect. 3 and the distances are normalised to the clusters' r_h. We computed the Kolmogorov–Smirnov statistic on the samples of BSS and REF stars in both clusters to test whether the two samples are drawn from the same parent distribution. The KS test gives a p-value of well below 1% in both cases. This fact implies that we can safely reject the hypothesis that the BSS and the REF samples come from the same parent population.

In order to further quantify the difference between the distributions of the two populations, we calculate A^+ following the recipe by Ferraro et al. (2018). In particular, the choice of estimating the A^+ when the radial distributions are normalised to the r_h of their respective cluster makes it possible to perform a direct comparison of the A^+ of Rup 106 and IC 4499 with that of the clusters studied in Ferraro et al. (2018). We find A^+ to be 0.111 ± 0.027 and 0.079 ± 0.011 for Rup 106 and IC 4499, respectively. Errors on A^+ were obtained using the jackknife bootstrapping technique (Lupton 1993; see also Dalessandro et al. 2019). The A^+ values derived in this work for Rup 106 and IC 4499 can then be directly compared to the large compilation of clusters studied in Ferraro et al. (2018) in order to constrain the dynamical age of the target clusters.

Figure 8 compares the values of A^+ for the 48 GCs published in Ferraro et al. (2018; black solid circles), Rup 106, and IC 4499 (red solid circles) against the number of core relaxation times (t_{rc}) that have occurred since the epoch of cluster formation ($t_{GC} = 12$ Gyr): $N_{relax} = t_{GC}/t_{rc}$. To the same plot we add the A^+ obtained using the BSS population of the Halo GCs AM1, Eridanus, Pal 3, and Pal 4 (solid star-like points) published in Beccari et al. (2012).

As already explained in Ferraro et al. (2018), we observe a clear correlation between the value of A^+ and N_{relax}, with the value of A^+ of a GC increasing as the cluster evolves dynamically. This is clearly demonstrated by the fact that the cluster in the top right corner of Fig. 8, namely that with the biggest value of A^+, is M 30 which has shown empirical signatures of having experienced the collapse of the core (see Ferraro et al. 2009). On the contrary, the cluster with the smallest value of A^+, in the bottom left of Fig. 8, is OmegaCen, which has been shown to not be fully relaxed even in the central regions (Ferraro et al. 2006).

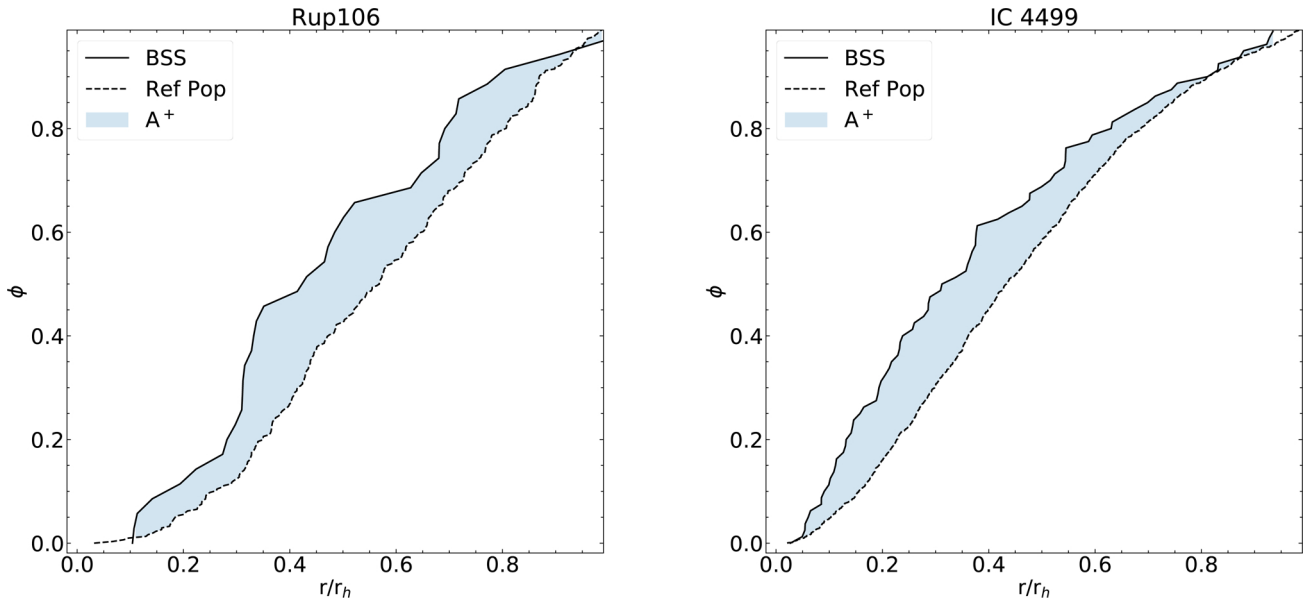

Fig. 7. Estimation of A^+. Cumulative radial distributions of the stars in Rup 106 and IC 4499 (*left* and *right panels*, respectively) belonging to the BSS and REF populations, the latter taken as representative of the distribution of the light of the clusters. The radial distributions are normalised to the clusters' r_h.

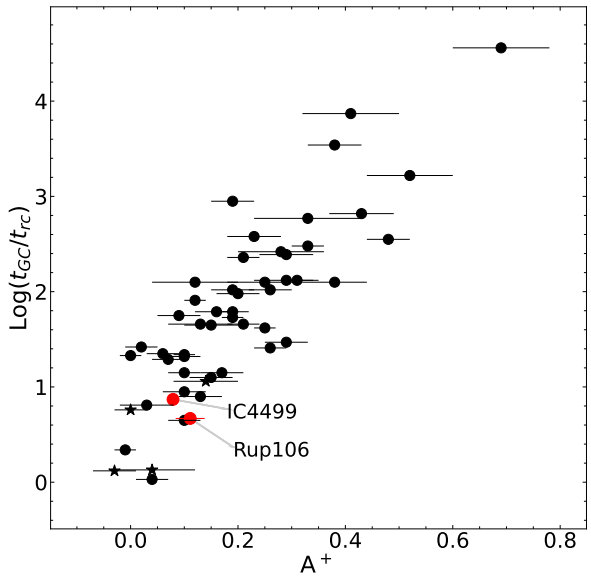

Fig. 8. Dynamical clock. The value of A^+ calculated for Rup 106 and IC 4499 (red solid circles), the GC studied in Ferraro et al. (2018; black filled circles) and the Halo GCs AM1, Eridanus, Pal 3, and Pal 4 (solid star-like points) studied in Beccari et al. (2012) as a function of the logarithm of the cluster core relaxation times (t_{rc}) that have occurred since the epoch of cluster formation t_{GC} = 12 Gyr.

Clearly the values of A^+ of Rup 106 and IC 4499 nicely follow the observed trend. Interestingly, the four Halo GCs studied in Beccari et al. (2012) and shown on this plot as solid star-like points share similar properties with respect to Rup 106 and IC 4499, all being younger (by 10–11 Gyr) and slightly less massive than the bulk of the GCs in the Galaxy (see Beccari et al. 2012, for a detailed discussion). The plot in Fig. 8 demonstrates that the dynamical history of this family of GCs, as imprinted in the radial distribution of the BSSs, nicely resembles that of the whole family of Galactic GCs. While we discuss the possible implication of this result with respect to the origin of these GCs below, it is worth mentioning here that, given the large distance of these Halo GCs (>50 kpc from the Galactic centre), it is impossible to resolve the low-mass stellar populations in these clusters and hence sample the MS MF to study the degree of mass segregation. The A^+ is therefore the only empirical method allowing us to investigate the dynamical age of these remote GCs. More specifically, we find the A^+ values derived for Rup 106 and IC 4499 to be in very good agreement with those of dynamically young clusters.

5. The deep sample: radial distribution of the mass function

To further investigate the mass segregation phenomenon in Rup 106 and IC 4499, we analysed the radial variation of the MF of the MS stars. Studying the shape of the MF in different regions of the clusters provides information about the effect of cluster internal dynamics on stars in a wide range of masses, including the faint end of the MS where most of the cluster mass lies. In relaxed stellar systems, the slope of the MF is expected to vary as a function of the distance from the cluster centre, with indexes decreasing as the distance increases, because of the differential effect of mass segregation.

As shown in Fig. 1, the ACS images alone allow us to fully sample the core region in both the clusters. Ideally, in order to fully appreciate the change in the slope of α, it is important to derive the MF for as large a fraction of the cluster extension as possible and always beyond the half-mass radius. In the case of Rup 106, the ACS images sample the cluster out to the half-mass radius while the latter falls outside of the ACS field of view in the case of IC 4499 (see Fig. 1). We therefore used photometry obtained from a set of HST WFC3 parallel observations (Sect. 2) in order to sample the MS stars in IC 4499 beyond the half-mass radius.

The HST data used in this paper were used by Dotter et al. (2011) to study the age and metallicity of six halo GCs, including Rup 106 and IC 4499. The authors performed a detailed study of the age of the clusters via isochrone fitting, following

Table 2. Best-fit parameters of the isochrone fitting from Dotter et al. (2011).

Cluster	$(m-M)_V$	$E(B-V)$	[Fe/H]	[α/Fe]	Age (Gyr)
IC 4499	17.07	0.18	−1.6	0.2	12.0 ± 0.75
Rup 106	17.12	0.14	−1.5	0.0	11.5 ± 0.5

the recipe from Dotter et al. (2010). In our work, we therefore adopted the models from Dotter et al. (2008) and the best-fit isochrone parameters reported in Table 3 of Dotter et al. (2011). For completeness, we report the parameters here in Table 2. Figure 9 shows the best-fit isochrones for both clusters (black lines), where the open squares indicate the mean-ridge line of the MS and the associated 1σ uncertainty. Figure 9 clearly demonstrates the exquisite fits of the MS obtained using the mentioned isochrones and distance and reddening values. We also highlight the range of masses covered by the data. As discussed in Sect. 2.2, the quality of the adopted images allows us to sample the MS stars with a photometric completeness of better than 80% down to $V = 27.5$ mag. This corresponds to a capability of sampling the MS in a broad range of masses, down to the very low-mass regime of 0.25 $M_\odot$ (see Fig. 9).

The MF is calculated for each cluster using the stars along the MS in each case. We selected all the stars lying at a distance from the MS mean-ridge lines in the $V-I$ colour of $<2\sigma$ of the uncertainty of the line itself. This approach allows us to exclude the majority of unresolved binaries, which are well known to populate a secondary sequence parallel to the MS at a maximum distance of 0.75 mag in the $V-I$ colour (see e.g., Sollima et al. 2008). We note that a fraction of binaries might indeed still be included in the selection. Still, those are binaries with a very low mass ratio and whose luminosity is entirely dominated by the more massive primary. There is therefore no significant impact of unresolved binaries on the derivation of MFs.

Using the detailed information given in Fig. 4, we assigned a completeness factor of $\phi_\star$ to each star of a given V mag and position on the sky by interpolating the appropriate completeness curves. We then used the mass-to-light conversion available on the adopted best-fit isochrones from Dotter et al. (2008) to convert the V magnitudes of the stars previously selected along the MS into stellar mass.

We binned the stars in the stellar masses range $0.25 \leq M_\odot \leq 0.75$ adopting a step of 0.1 $M_\odot$. The total number of stars in a given bin of mass is calculated as $N_{\rm corr} = \sum_i^{N_{\rm obs}} \phi_{\star_i}^{-1}$ while the associated error is $\sigma_{N_{\rm corr}} = \sqrt{\sum_i^{N_{\rm obs}} (\sigma_{\phi_{\star_i}}/\phi_{\star_i})^2}$. This way we are able to build a completeness-corrected MF taking into account the incompleteness effects. In order to estimate the level of contamination on each bin of mass from background and foreground stars, we downloaded a catalogue of simulated stars in the V and I Johnson-Cousin magnitudes from the Besançon Galaxy Model (Robin et al. 2003), sampling the Galaxy stellar population in a 1 deg^2 area around the two clusters. We selected the synthetic stars along the MSs of the clusters as done with the real stars and converted their V magnitudes into masses using the same best-fit isochrones described above. This allows us to remove from the observed MF the contribution from fore/background objects.

Figure 10 shows the final MFs for each cluster measured inside concentric rings, sampling different distances. The best fit to each MF is shown as a dashed line. The slopes of the fits are used as the slope of the MF and are also reported in the plots. We reiterate here that in our notation, the Salpeter IMF would have a slope $\alpha = -2.35$, and that a positive index implies that the number of stars decreases with decreasing mass. In the case of Rup 106, α ranges from −0.2 in the core of the cluster to −1.2 in the most external region sampled with the ACS data, that is, up to 100″ or $\sim 2r_{\rm c}$. We note here that the radial extension of the external annulus is such that it includes the $r_{\rm h} = 88\farcs83$ of the cluster. The radial behaviour of the MF in IC 4499 changes from $\alpha = 0.3$ in the centre to −1.9 in the external region.

Clearly, in both clusters, the slope of the MF α significantly changes as a function of the distance from the cluster centre. Because of equipartition of energy, massive stars tend to have a smaller velocity dispersion than the average and, as they occupy smaller orbits, are found closer to the cluster centre, generating mass segregation. The value of α becomes more negative while moving towards the external regions of the clusters, which is a consequence of the fact that the proportion of massive stars is higher in the centres of the clusters. This fact confirms that a certain level of mass segregation is detected in both clusters. This result is qualitatively in agreement with what was found using the BSS radial distribution.

6. Discussion and conclusion

In this work, we used a combination of high-resolution HST data and photometric catalogues from ground-based wide-field telescopes to study the dynamical state and age of the globular clusters Rup 106 and IC 4499. In particular, using ground-based catalogues combined with short-exposure HST images of the cores of the clusters, we derived the radial-density profiles of the clusters from detailed star counts (see Fig. 5). We show that the profiles are well reproduced by King models and we provide new estimates of the structural parameters of both clusters.

In addition, we use the same catalogues to homogeneously select the population of BSS stars over the total extension of the clusters. We compared the radial distribution of the BSSs to that of a selection of stars along the MS turn-of, which we used as a reference population (REF), that is, a population sampling the normal distribution of the stars in the clusters. We used the parameter A^+, defined as the area between the cumulative distribution of the BSS and the REF populations (see Fig. 7), to empirically constrain the dynamical age of Rup 106 and IC 4499. In Fig. 8 we show the distribution of the A^+ of Rup 106 and IC 4499 together with that of several galactic GCs studied by Ferraro et al. (2018) as a function of the relaxation times of the clusters at their core radius. This plot allows us to evaluate empirically the dynamical age of the two clusters studied in this paper. Figure 8 reveals that in both Rup 106 and IC 4499, two-body relaxation has only very recently started to efficiently sink the massive stars towards the central regions. Therefore, both clusters can be classified as dynamically young.

The radial variation of the slopes of the MF α for each cluster measured in the mass range $0.25 \leq M_\odot \leq 0.75$ also indicates that two-body relaxation has efficiently started to affect the distribution of the stars there. In particular, the value of α changes from -0.1 ± 0.1 and 0.3 ± 0.2 in the central area of Rup 106 and IC 4499, respectively, to -1.2 ± 0.1 and -1.9 ± 0.2 in the external regions. As explained in the previous section, a progressively more negative (positive) α slope indicates a decrease (increase) in the proportion of massive stars with respect to low-mass stars. Therefore, the radial change of α indicates the presence of a certain degree of mass segregation in both clusters. It is worth mentioning that in the case of Rup 106, we are able to sample the

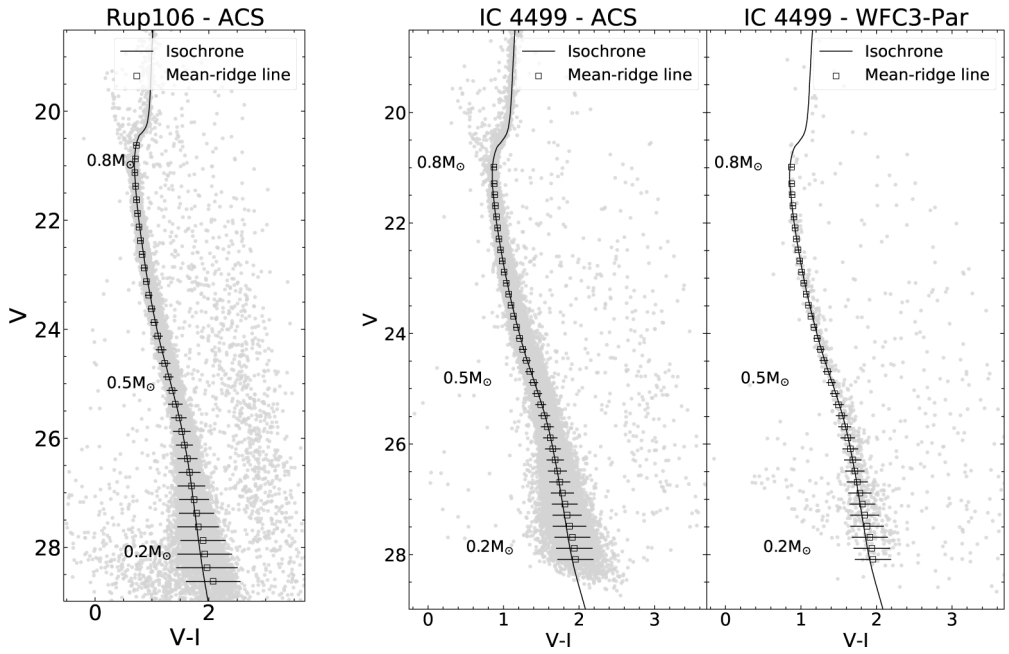

Fig. 9. CMD of the HST data for Rup 106 and IC 4499 (*left* and *right bi-panels*, respectively). The ACS data used to sample the core region are complemented with a catalogue obtained with ACS and WFC3 parallel observations for Rup 106 and IC 4499, respectively. The open squares indicate the mean ridge lines of the clusters, while the solid curve shows the best-fit isochrones.

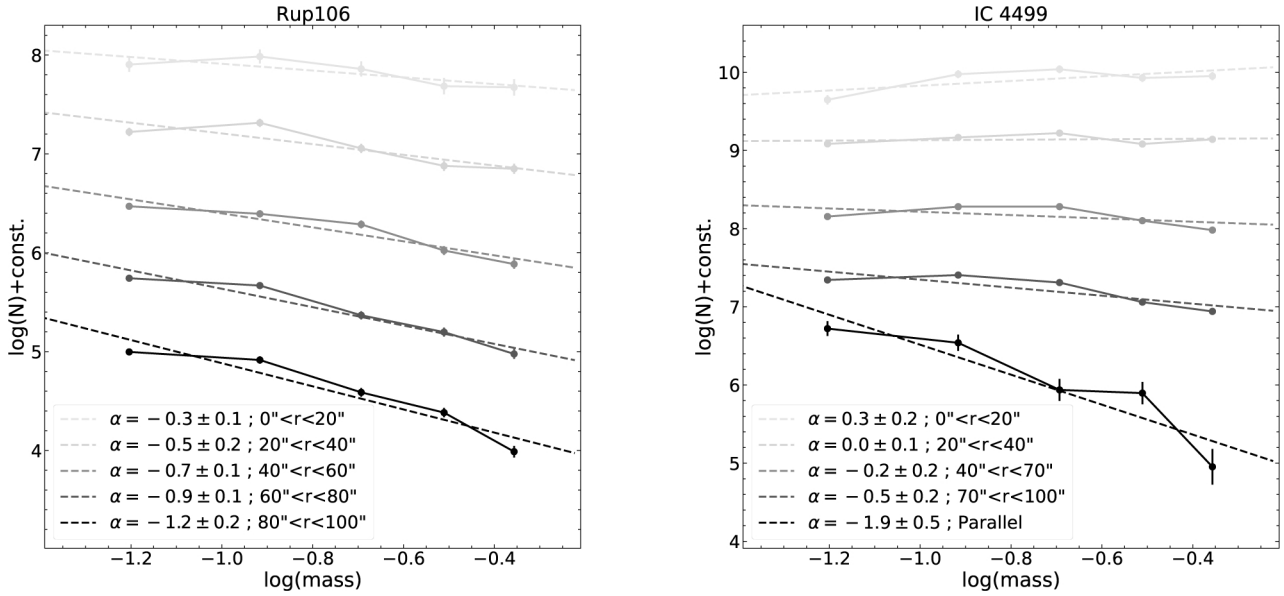

Fig. 10. Cluster completeness-corrected MFs calculated at different radial annuli from the cluster centres. The dashed line indicates the fit to the MF. The slopes of the fits indicate the slope of the MF and are also indicated in the plots. We reiterate here that in our notation, the Salpeter IMF would have a slope $\alpha = -2.35$, and that a positive index implies that the number of stars decreases with decreasing mass.

MF out to $\sim 2 \times r_c$ reaching the cluster's $r_h = 88\farcs83$, while in the case of IC 4499, α is estimated out to $\sim 5 \times r_c$ or $\sim 2 \times r_h$.

The close agreement between the different mass segregation indicators used in this work for Rup 106 and IC 4499 (see also Bellazzini et al. 2012; Dalessandro et al. 2015 for the cases of NGC 2419 and NGC 6101) provides further support to the use of the radial distribution of BSSs as a powerful indicator of the dynamical evolution of stellar systems (e.g., Ferraro et al. 2012, 2018). Indeed, the use of BSSs is convenient as they are significantly brighter with respect to the MS stars, they are easy to identify with a high level of completeness and with short exposure times, and their use to asses the degree of mass segregation (the radial distribution) is free from theoretical assumptions from stellar evolution models. Therefore, the BSS radial distribution represents the clearest indicator of mass segregation in dense stellar systems. The plot in Fig. 8 not only indicates (in agreement with the radial distribution of α) the presence of mass segregation, but also demonstrates that two-body relaxation has only very recently started to efficiently act in Rup 106 and IC 4499.

Our study indicates that, from a strictly dynamical perspective, the behaviour of both clusters is identical when compared to those of the GCs in the Milky Way (MW; see Fig. 8). As mentioned in Sect. 4, the A^+ of the Halo GCs AM1, Eridanus, Pal 3, and Pal 4 (solid star-like points in Fig. 8) indicates that

all these clusters show a dynamical history (as imprinted in the BSS radial distribution) that is highly comparable to those of any other Galactic GC. Specifically, while all these clusters are slightly younger (10–11 Gyr) in terms of the absolute age of the stellar population and with respect to the majority of GCs in the Galaxy, they are all also young from a dynamic perspective, as shown by their location on the plot in Fig. 8.

Interestingly, Dalessandro et al. (2018) discovered the presence of a mild spread in N and Na abundance among the RGB of IC 4499, which they interpreted as a signature of the presence of multiple stellar populations in the cluster. While it is well established that the stellar populations in GCs exhibit intrinsic star-to-star variations in their light-element abundances (see e.g., Carretta & Bragaglia 2021, and references), it is still not clear why Rup 106 does not show any chemical signature that would indicate the presence of multiple stellar populations (Frelijj et al. 2021). Currently, despite efforts, no spectroscopic studies have been able to prove the presence of multiple stellar populations in the other halo GCs mentioned above with robust statistical evidence (see e.g., Koch et al. 2009; Koch & Côté 2010). Clearly, our study suggests that the absence of multiple stellar populations in Rup 106 is not due to a peculiar dynamical history of the cluster.

Interestingly, Baumgardt & Hilker (2018) indicates that IC 4499 has the highest initial total mass among the whole group mentioned above ($M = 10^{5.53}\ M_{\odot}$). Rup 106 has a predicted initial total mass of $10^{5.12}\ M_{\odot}$ while AM1, Eridanus, Pal 3, and Pal 4 have initial total masses of lower than $10^{5}\ M_{\odot}$. While we exclude any peculiar dynamical history for all these clusters with the present study, we at the same time seem to give further support to the hypothesis that whether or not a cluster hosts multiple stellar populations primarily depends on its mass and stellar density (see e.g., Bastian & Lardo 2018). However, abundance ratios for individual stars in the halo GCs are urgently needed to assess the presence of multiple stellar populations in these clusters and ultimately understand the relationship investigated by recent studies (see e.g., Massari et al. 2019; Malhan et al. 2021) between remote GCs and other halo substructures (i.e., luminous and ultra-faint dwarf spheroidal galaxies).

Acknowledgements. We thank the referee Christian Moni Bidin for their time and a helpful report that has improved this paper. MC, ED acknowledge financial support from the project Light-on-Dark granted by MIUR through PRIN2017-2017K7REXT. Based on observations made with the NASA/ESA *Hubble* Space Telescope, obtained from the data archive at the Space Telescope Science Institute. STScI is operated by the Association of Universities for Research in Astronomy, Inc. under NASA contract NAS 5-26555. This work has made use of data from the European Space Agency (ESA) mission *Gaia* (`https://www.cosmos.esa.int/gaia`), processed by the *Gaia* Data Processing and Analysis Consortium (DPAC, `https://www.cosmos.esa.int/web/gaia/dpac/consortium`). Funding for the DPAC has been provided by national institutions, in particular the institutions participating in the *Gaia* Multilateral Agreement. This research has made use of the products of the Cosmic-Lab project funded by the European Research Council.

References

Alessandrini, E., Lanzoni, B., Ferraro, F. R., Miocchi, P., & Vesperini, E. 2016, ApJ, 833, 252
Bailyn, C. 1995, ARA&A, 33, 133
Bastian, N., & Lardo, C. 2018, ARA&A, 56, 83
Baumgardt, H., & Hilker, M. 2018, MNRAS, 478, 1520
Baumgardt, H., Hilker, M., Sollima, A., & Bellini, A. 2019, MNRAS, 482, 5138
Beccari, G., Ferraro, F., Possenti, A., et al. 2006, AJ, 131, 2551
Beccari, G., Lützgendorf, N., Olczak, C., et al. 2012, ApJ, 754, 108
Bellazzini, M., Fusi Pecci, F., Messineo, M., Monaco, L., & Rood, R. T. 2002, AJ, 123, 1509
Bellazzini, M., Dalessandro, E., Sollima, A., & Ibata, R. 2012, MNRAS, 423, 844
Buonanno, R., Buscema, G., Fusi Pecci, F., Richer, H. B., & Fahlman, G. G. 1990, AJ, 100, 1811
Buonanno, R., Corsi, C. E., Fusi Pecci, F., Richer, H. B., & Fahlman, G. G. 1993, AJ, 105, 184
Cadelano, M., Dalessandro, E., Webb, J. J., et al. 2020, MNRAS, 499, 2390
Carretta, E., & Bragaglia, A. 2021, A&A, 646, A9
Dalessandro, E., Ferraro, F. R., Massari, D., et al. 2013, ApJ, 778, 135
Dalessandro, E., Ferraro, F. R., Massari, D., et al. 2015, ApJ, 810, 40
Dalessandro, E., Lardo, C., Cadelano, M., et al. 2018, A&A, 618, A131
Dalessandro, E., Cadelano, M., Vesperini, E., et al. 2019, ApJ, 884, L24
Dotter, A., Sarajedini, A., & Yang, S.-C. 2008, AJ, 136, 1407
Dotter, A., Sarajedini, A., Anderson, J., et al. 2010, ApJ, 708, 698
Dotter, A., Sarajedini, A., & Anderson, J. 2011, ApJ, 738, 74
Erben, T., Schirmer, M., Dietrich, J. P., et al. 2005, Astron. Nachr., 326, 432
Ferraro, I., Ferraro, F. R., & Fusi Pecci, F. 1995, MNRAS, 275, 1057
Ferraro, F., Sollima, A., Rood, R., et al. 2006, ApJ, 638, 433
Ferraro, F. R., Beccari, G., Dalessandro, E., et al. 2009, Nature, 462, 1028
Ferraro, F. R., Lanzoni, B., Dalessandro, E., et al. 2012, Nature, 492, 393
Ferraro, F. R., Lanzoni, B., Raso, S., et al. 2018, ApJ, 860, 36
Fiorentino, G., Lanzoni, B., Dalessandro, E., et al. 2014, ApJ, 783, 34
Frelijj, H., Villanova, S., Muñoz, C., & Fernández-Trincado, J. G. 2021, MNRAS, 503, 867
Fusi Pecci, F., Bellazzini, M., Cacciari, C., & Ferraro, F. R. 1995, AJ, 110, 1664
Gaia Collaboration (Prusti, T., et al.) 2016, A&A, 595, A1
Gaia Collaboration (Brown, A. G. A., et al.) 2018, A&A, 616, A1
Harris, W. E. 1996, AJ, 112, 1487
King, I. R. 1966, AJ, 71, 64
Knigge, C., Leigh, N., & Sills, A. 2009, Nature, 457, 288
Koch, A., & Côté, P. 2010, A&A, 517, A59
Koch, A., Côté, P., & McWilliam, A. 2009, A&A, 506, 729
Lanzoni, B., Ferraro, F. R., Alessandrini, E., et al. 2016, ApJ, 833, L29
Lanzoni, B., Ferraro, F. R., Dalessandro, E., et al. 2019, ApJ, 887, 176
Leigh, N., Knigge, C., Sills, A., et al. 2013, MNRAS, 428, 897
Leonard, P. J. T. 1996, ApJ, 470, 521
Lombardi, J. C. J., Rasio, F. A., & Shapiro, S. L. 1995, ApJ, 445, L117
Lupton, R. 1993, Statistics in Theory and Practice (Princeton: Princeton University Press)
Malhan, K., Yuan, Z., Ibata, R. A., et al. 2021, ApJ, 920, 51
Mapelli, M. 2018, arXiv e-prints [arXiv:1807.07944]
Massari, D., Koppelman, H. H., & Helmi, A. 2019, A&A, 630, L4
Meylan, G., & Heggie, D. C. 1997, A&A, 8, 1
Miocchi, P. 2006, MNRAS, 366, 227
Miocchi, P., Lanzoni, B., Ferraro, F. R., et al. 2013, ApJ, 774, 151
Prager, B. J., Ransom, S. M., Freire, P. C. C., et al. 2017, ApJ, 845, 148
Raso, S., Libralato, M., Bellini, A., et al. 2020, ApJ, 895, 15
Robin, A., Reylé, C., Derrière, S., & Picaud, S. 2003, A&A, 409, 523
Schirmer, M. 2013, ApJS, 209, 21
Sills, A., Glebbeek, E., Chatterjee, S., & Rasio, F. A. 2013, ApJ, 777, 105
Singh, G., & Yadav, R. K. S. 2019, MNRAS, 482, 4874
Sirianni, M., Jee, M. J., Benítez, N., et al. 2005, PASP, 117, 1049
Sollima, A., Lanzoni, B., Beccari, G., Ferraro, F. R., & Fusi Pecci, F. 2008, A&A, 481, 701
Stetson, P. B. 1987, PASP, 99, 191
Stetson, P. B. 1994, PASP, 106, 250
Stetson, P. B., Pancino, E., Zocchi, A., Sanna, N., & Monelli, M. 2019, MNRAS, 485, 3042
Villanova, S., Geisler, D., Carraro, G., Moni Bidin, C., & Muñoz, C. 2013, ApJ, 778, 186
Walker, A., & Nemec, J. M. 1996, AJ, 112, 2026
Walker, A., Kunder, A., Andreuzzi, G., et al. 2011, MNRAS, 415, 643
Webb, J. J., Vesperini, E., Dalessandro, E., et al. 2017, MNRAS, 471, 3845
Zacharias, N., Finch, C. T., Girard, T. M., et al. 2012, VizieR Online Data Catalog: I/322A